Interaction Noise from Tandem Landing Gear Wheels with Hub and Rim Cavities

Meng Wang[*], David Angland[†]

Faculty of Engineering and the Environment

University of Southampton, Southampton, SO16 7QF, UK.

Aline Scotto[‡]

Acoustics Department, Airbus

316 route de Bayonne, 31060 Toulouse Cedex 09, France

Wheels are major noise sources on landing gears. Accurate numerical predictions of wheel noise can provide insights into landing gear noise generation mechanisms and help improve landing gear noise prediction models. Previous simulations have been conducted on an isolated high-fidelity wheel model containing a tyre, a hub, a sidewall and two rim cavities. The hub cavity was an important middle frequency noise source due to the first and second hub cavity depth modes, and the rim cavities were major high frequency noise sources. This work investigates the major noise sources in different frequency ranges of two tandem wheels, with the same geometry as the previous isolated wheel case, by performing high-order numerical simulations at $M = 0.23$. This paper focuses on the mechanisms and characteristics of the wheel interaction noise. The aerodynamic results are validated against experiments and demonstrate reasonable agreements. The flow interactions are found to be mainly in the side direction with a spectral peak in the side force at a Strouhal number of 0.19, based on the wheel width, which is due to a flapping shear layer mode in the gap. The downstream wheel is the major noise source and has a favourable sound radiation direction to the sideline. The effects of the downstream wheel hub and rim cavities are isolated by covering them in the simulations. The flow interactions dominate the hub cavity depth modes in the generation of middle frequency downstream wheel noise. For high frequency noise, covering both the hub and rim cavities on the downstream wheel only, reduced the noise radiated towards the ground. This high frequency noise reduction was not achieved when the hub cavity alone was covered.

Nomenclature

Symbols

c	Speed of sound	Re	Reynolds number
C_D	Drag coefficient	T	Temperature
C_L	Lift coefficient	u, v, w	Velocity components in the x, y and z directions
C_p	Pressure coefficient		
C_S	Side force coefficient	W	Wheel width
D	Wheel diameter	x, y, z	Cartesian coordinates system
M	Mach number		
p	Pressure	**Greek**	
		ϕ	Azimuthal angle

[*]PhD Student, Airbus Noise Technology Centre, mw3g13@soton.ac.uk.

[†]Associate Professor, Airbus Noise Technology Centre, AIAA Member, d.angland@soton.ac.uk.

[‡]Acoustic Engineer, Acoustics Department, Airbus.

American Institute of Aeronautics and Astronautics

ψ	Polar angle		CADWIE	Control of Approach Drag Without
ρ	Density			Impact on the Environment
θ	Axial angle		DDES	Delayed Detached Eddy Simulation
			DW	Downstream Wheel
Subscripts			FFT	Fast Fourier Transform
			FW-H	Ffowcs-Williams and Hawkings
∞	Freemstream quantity		OASPL	OverAll Sound Pressure Level
			PSD	Power Spectral Density
			RMS	Root Mean Square
Superscripts			S-A	Spalart-Allmaras
$+$	Wall unit		SPL	Sound Pressure Level
rms	Root mean square		SW	Single Wheel
			TSB	Technology Strategy Board
			UW	Upstream Wheel
Abbreviations			ZCBC	Zonal Characteristic Boundary
BC	Boundary Condition			Condition

I.   Introduction

Landing gears are recognized as one of the most significant contributors to airframe noise for commercial aircraft in the approach configuration.[1] Wheels are the major contributors to the landing gear noise.[2,3] Several experimental and numerical tests have been performed to study the flow features and far-field acoustics of landing gear wheels. Casalino *et al.*[4] numerically investigated the noise from two facing wheels with rim cavities on the LAGOON (LAnding Gear nOise database for CAA validatiON)[5] landing gear geometry. Two tonal peaks were found in the sideline direction due to the wheel cavity resonances. Zhang *et al.*[6] performed aerodynamic and aeroacoustic experiments of an isolated high-fidelity landing gear wheel. They found that the wheel noise is characterized by broadband middle frequency noise centred around 630 Hz and 1250 Hz. Wang *et al.*[7,8] conducted numerical simulations with the same geometry used by Zhang *et al.*[6] and found that the noise at 630 Hz and 1250 Hz is generated by the first and second depth modes of the hub cavity. However, these previous works have not considered the interaction noise from wheels in tandem, which is significant for four-wheel and six-wheel landing gear noise.

Flow interactions can occur for wheels in a tandem configuration. A benchmark case of tandem cylinders, with a separation distance of $L = 3.7D$ (where D is the diameter of the wheel), was proposed to represent tandem landing gear wheels.[9] In the experiment of this benchmark case, a co-shedding state was found with both cylinders shedding vortices.[9] The downstream cylinder was demonstrated to be the dominant noise source, which is characterised with tonal noise at the shedding frequency. For a typical landing gear, the separation distance of the tandem wheels is between $1.1D$ and $1.5D$,[10] and in such a range, the shear layer from the upstream cylinder is expected to reattach on the downstream cylinder,[11,12,13,14] and no regular shedding can be observed. Additionally, wheels can be considered as circular cylinders of short aspect ratios, the flow field surrounding which is more complex compared to the large aspect ratio circular cylinders. Thus, the tandem landing gear wheels noise is expected to be more broadband. Spagnolo *et al.* experimentally[10] and numerically[15] studied the aerodynamic loads of a tandem wheel case, with three separation distances, i.e. $1.1D$, $1.3D$ and $1.5D$. The wheels are simplified by short circular cylinders. They found a general trend of higher mean drag coefficient and a lower RMS of force coefficients with increasing separation distance.

Despite the previous investigations of aerodynamic and aeroacoustic behaviour of tandem cylinders flow and aerodynamic loads of tandem wheels flow, the noise from tandem landing gear wheels, especially with realistic wheel geometries, has not been studied separately. In this paper, the interaction noise between two wheels in tandem at $L = 1.5D$ will be investigated. The wheels have a detailed geometry including a hub and rim cavities, which is the same as the one used in the experiment by Zhang *et al.*[6] This paper is structured in the following manner. The wheel geometry and the grid generation are provided in Section II. Section III describes the numerical method and the computational setup in the simulations. The aerodynamic and acoustic simulation results are provided in Section IV, together with comparisons to the experimental data by Spagnolo *et al.*[16] The results are compared to the isolated wheel and the effect of covering the hub and rim cavities on the downstream wheel is also investigated. The summary of this paper is given in Section V.

II.   Model detail and computational grids

The wheels used in this work are 33% scaled isolated landing gear wheels from the TSB CADWIE (Control of Approach Drag Without Impact on the Environment) project, which are illustrated in Figure 1. The diameter of the wheel and the width of the shoulder are $D = 480$ mm and $W = 186$ mm, respectively. The isolated wheel contains a sidewall and a hub on two different sides. A large shallow cylindrical cavity with a diameter-to-depth ratio of approximately 0.3 is located around the hub. Surrounding the sidewall and the hub cavity are two rim cavities, the depth of which are approximately $0.045D$. This wheel geometry is the same with the previous isolated single wheel numerical studies by Wang et al.[7,8] and experimental investigations by Zhang et al.[6] In the current simulation, the two wheels are inline with a separation distance of $L = 1.5D$, and the angle of attack is $0°$.
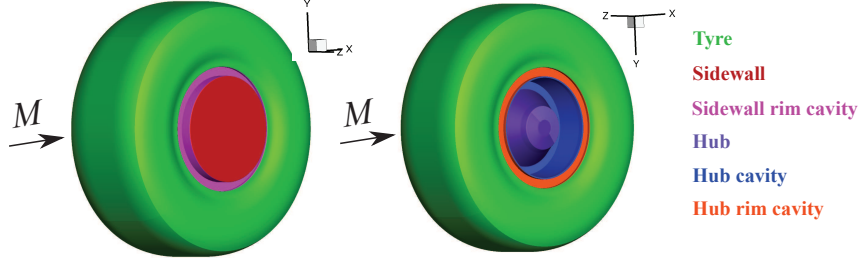

Figure 1. The geometry of the CADWIE wheel in the simulations.

The numerical simulations were performed on multi-block structured grids. The computational domain extends $5D$, $4D$ and $16D$ in the upstream, above and below, and downstream directions, respectively, from the centre of the upstream wheel. The spanwise length of the domain is $8D$. This computational domain is the same with the one used in the isolated single wheel simulations by Wang et al.[7] In the boundary layer region, the value of the wall distance y^+ is less than 2.0 and a grid stretching ratio of 1.15 in the wall normal direction is used to relax the grid distribution. The hub cavity walls are meshed by a cylindrical grid with 300, 150 and 85 grid points in the azimuthal, radial and depth directions. The same mesh resolution is used in the sidewall region. There are 60 grid points distributed along the width of the wheel. A grid sensitivity was performed by Wang et al.,[7] and showed that this grid resolution was adequate to provide good agreement to the aerodynamic and acoustic experimental results. The detailed mesh topology and grid distributions were described by Wang et al.[7,8]

III.   Numerical methods and computational setup

The simulations were performed using a high-order finite-difference solver, known as SotonCAA. The three-dimensional Navier-Stokes equations are solved with the Delayed Detached Eddy Simulation (DDES) turbulence model[17] in generalized coordinates using high-order optimized penta-diagonal finite-difference schemes.[18] Compact filters[19] are used for numerical stability. At block interfaces, a finite volume method is applied to reduce grid-induced errors.[20] The inflow boundary condition is provided by the far-field Riemann pressure condition and a Zonal Characteristic Boundary Condition (ZCBC)[21] is applied at the outflow edge. No-slip isothermal wall boundary conditions are imposed on the wheel surface. A second-order implicit time-stepping method with Newton-like subiterations is used to march the solution in time.[22] The far-field acoustics are computed using the Ffowcs-Williams and Hawkings (FW-H) method, based on the Farassat 1A formulation.[23] The FW-H integral surface in the simulations is positioned on the surface of the CADWIE wheel. The solid FW-H integral surface can reduce the risk of noise contamination by large vortical wave fluctuations passing through the surface.[24]

The freestream quantities are $\rho_\infty = 1.22$ kg/m^3, $p_\infty = 99456$ Pa and $T_\infty = 288.16$ K, $M_\infty = 0.23$. The eddy viscosity ratio at the inlet is 5. The corresponding Reynolds number is $Re = 2.5 \times 10^6$ based on the wheel diameter D. The time step size for the simulations is 6×10^{-7} seconds. The flow was fully developed after a convective time of approximately 20 wheel diameters, after which the flow data were collected for 0.6 seconds (approximately 100 wheel diameters for the convective time).

American Institute of Aeronautics and Astronautics

IV. Results

IV.A. Instantaneous flow field

The instantaneous $Q-$criterion is shown in Figure 2. The gap region is dominated by large-scale structures that are due to flow separations from the upstream wheel. The wake of the upstream wheel then impinges on the downstream wheel. The front face of the downstream wheel is shown to be surrounded by large-scale flow structures. Since the flow field around the downstream wheel contains more large-scale turbulent structures, the downstream wheel is expected to be the dominant noise source, which should be characterised by low frequency interaction noise.
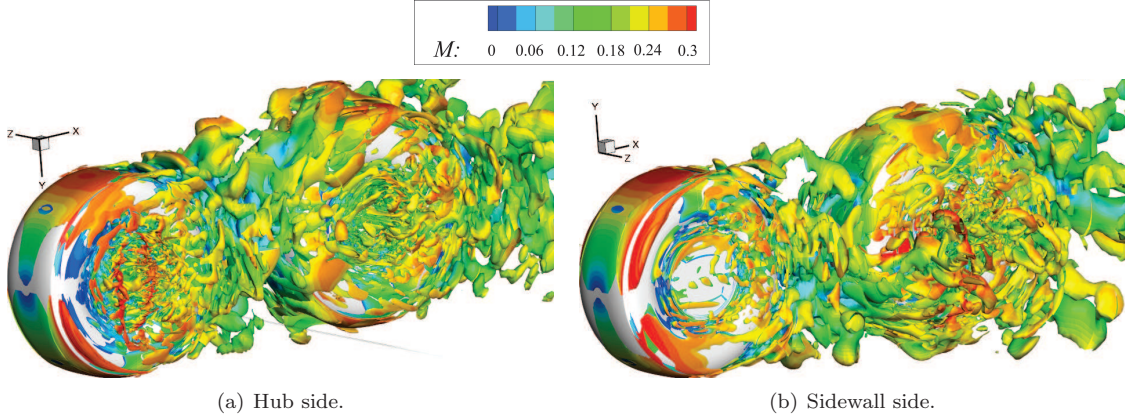

$M:$ 0 0.06 0.12 0.18 0.24 0.3

(a) Hub side.　　　　　　　　　　　　　　　(b) Sidewall side.

Figure 2. Instantaneous iso-contour of $Q = 10 \times U_\infty^2/D^2$ colored by the Mach number.

IV.B. Aerodynamic forces

The mean and RMS of the lift, drag and side force coefficients are given in Table 1, together with the isolated single wheel (SW) case by Wang *et al.*[8] The mean drag coefficient of the downstream wheel is approximately twice that of the upstream wheel, since the downstream wheel is immersed in the wake of the upstream wheel. The fluctuating side force C_S^{rms} dominates the lift C_L^{rms} and drag C_D^{rms} forces for the tandem wheels case. For a single isolated wheel, the fluctuating lift force C_L^{rms} dominates. This indicates that the flow interactions are mainly in the side direction, which can also be confirmed by the PSD levels of force coefficients against two Strouhal numbers based on the wheel diameter (St_D) and wheel width (St_W), in Figure 3. A spectral peak at $St_W = 0.19$ is shown for the side force C_S. This spectral peak in the side force is generated by the shear layer flapping in the gap and alternative impingements on the two side faces of the downstream wheel, at a frequency of $St_W = 0.19$, which will be shown in Section IV.C. In Table 1, a non-zero mean lift $\overline{C}_L$ is shown in both the isolated wheel case and the tandem wheels case, implying that the mean flow field is asymmetric. The downstream wheel produces much less mean lift compared to the upstream wheel, which is similar in magnitude to the isolated wheel, suggesting that the downstream wheel flow field is more effected by the flow interactions, which will be shown by the mean pressure coefficient distributions in Figure 6(b). Zdravkovich *et al.*[25] performed experiments to investigate the flow features past free-end circular cylinders with a spanwise length to diameter ratio W/D between 1 and 10, and an asymmetric flow pattern was found when $W/D < 3$. The asymmetry was demonstrated by Zdravkovich *et al.* to be bistable and can be biased to either side of the short span cylinder.[25] The same asymmetry was also found in the experiment of simplified tandem wheels by Spagnolo *et al.*[16] However, the mechanism of this asymmetry is still unclear.

IV.C. Shear layer flapping mode

The instantaneous streamwise velocity in the gap region on the $y/D = 0$ plane is shown in Figure 4. The separated shear layers from the upstream wheel form two large vortices, dominating the gap. P1 and P2 are two surface pressure monitors at the leading edges of the downstream wheel tyre where the shear layers directly impinge. Figure 5 shows the coherence of surface pressures at these two monitors. The coherence is

American Institute of Aeronautics and Astronautics

Case		$|\overline{C}_L|$	$\overline{C}_D$	$\overline{C}_S$	C_L^{rms}	C_D^{rms}	C_S^{rms}
Isolated single wheel[8]		0.022	0.237	0.019	0.030	0.010	0.019
	UW	0.219	0.217	0.024	0.017	0.020	0.038
Simulation	DW	0.018	0.426	0.013	0.033	0.038	0.075
	Total	0.201	0.643	0.037	0.035	0.036	0.082

Table 1. Summary of the force coefficients from the isolated single wheel (SW) case by Wang *et al.*,[8] the upstream wheel (UW), the downstream wheel (DW) and the total two wheels (Total) in the current tandem wheels case.

(a) Upstream wheel.

(b) Downstream wheel.
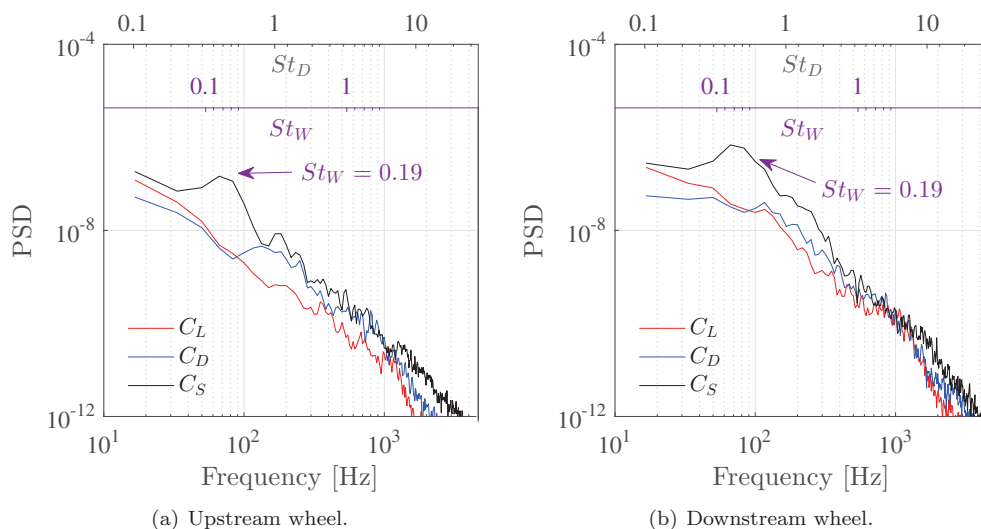
Figure 3. PSD of the force coefficients for the tandem wheels case.

noisier in the middle and high frequency ranges, due to the limited length of signal recorded in the numerical simulation. A strong coherence occurs at $St_W = 0.19$. The phase difference between the two surface pressures at $St_W = 0.19$, which was computed by applying the Fourier transform to each signal separately, is 173°, approximately a phase shift of 180°. This indicates that the shear layers impinge at the two downstream wheel leading edges alternatively at a shear layer flapping frequency of $St_W = 0.19$, which has also been shown by the plot of the side force coefficient in Figure 3.
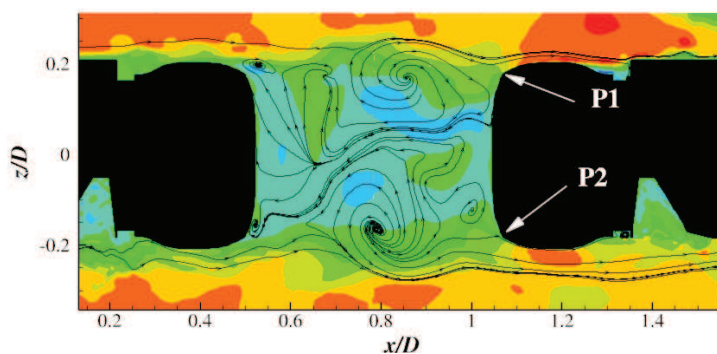

Figure 4. The instantaneous streamwise velocity in the range of $-0.15 < u/c < 0.3$, and the streamlines, on the $y/D = 0$ plane. P1 and P2 are two surface pressure monitors at the leading edge of the downstream wheel shoulder.

IV.D. Mean and RMS surface pressure coefficients

The mean and RMS pressure coefficients on the wheel centreline are compared with the experimental measurements by Spagnolo *et al.*[16] in Figures 6 and 7, respectively. No experimental data, with the same

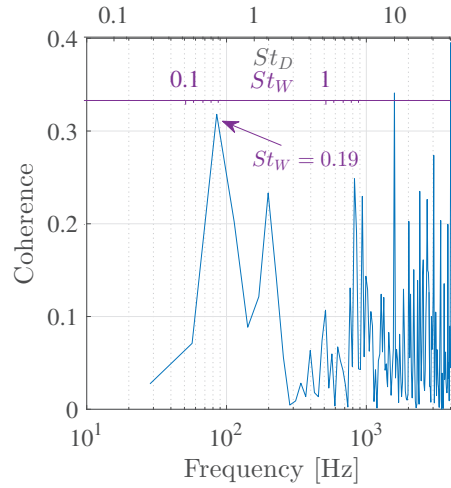American Institute of Aeronautics and Astronautics

Figure 5. The coherence between surface pressures monitored at two points (P1 and P2) at the leading edge of the downstream wheel in Figure 4.

wheel geometry and flow conditions as the current simulations, are available. The experiment by Spagnolo *et al.*[16] was performed at $Re = 5 \times 10^5$, and their measurements presented in the comparisons are with the upstream wheel boundary layer tripped with zigzag tape to produce a fully turbulent boundary layer. The current simulation simulates a fully turbulent boundary layer at $Re = 2.6 \times 10^6$. The wheel geometry used by Spagnolo *et al.*[16] is a simplified wheel without hub and rim cavities. As discussed in the isolated wheel case by Wang *et al.*,[8] the hub cavity and rim cavities have minor effects on the large-scale structures around the wheel, and those large scales dominate the RMS of surface pressure fluctuations. Additionally, the hub cavity and rim cavities are located at the side of the wheel. On the wheel centreline, the flow is less effected by the presence of hub and rim cavities. Thus, the distributions of C_p and C_p^{rms} on the wheel centreline in the current wheel configuration can be expected to be similar to the experimental measurements by Spagnolo *et al.*,[16] which are used to validate the simulation results.

In Figure 6 and 7, the observer angle (θ) is $0°$ at the upstream stagnation point and increases in a clockwise direction. A significant asymmetry is demonstrated in both the numerical and the experimental results. The stagnation point on the downstream wheel is at $\theta = 335°$. This asymmetry accounts for a highly non-zero mean lift coefficient in Table 1. The numerical predictions of C_p^{rms} are shown in Figure 7, and they show more discrepancies than C_p with the experiments. The discrepancies are likely due to the difference in the Reynolds number and state of the boudnary layer, which was artificially tripped in the experiments. Both of these can affect the separation points and subsequently the unsteady surface pressures. However, reasonable agreement in the levels and distribution patterns of C_p^{rms} is still achieved in the simulations.

IV.E. Far-field acoustics

The far-field acoustic observers are located at $25D$ from the upstream wheel centre. The observers are described by a polar angle ψ on the plane $y/D = 0$ and an azimuthal angle ϕ on the plane $x/D = 0$, which are defined in Figures 8(a) and 8(b), respectively. In the following discussions, the hub side observer, sidewall side observer and ground side observer refer to the positions of ($\psi = 90°$, $\phi = 180°$), ($\psi = 90°$, $\phi = 0°$) and ($\psi = 90°$, $\phi = 270°$). In the isolated wheel simulations by Wang *et al.*,[7,8] it has been found that the depth modes of the hub cavity are present in the far-field acoustics. The depth modes are given by,

$$f_i = \frac{ic}{4h'} \quad , \tag{1}$$

where c is the speed of sound, i is an integer. The effective depth h' taking account of the cavity opening is given by,[26]

$$h' = H_{\text{cavity}} + 0.8216 \frac{D_{\text{cavity}}}{2} \quad , \tag{2}$$

where H_{cavity} and D_{cavity} are the depth and diameter of the hub cavity. The first and second depth modes of the hub cavity in this geometry are 646 Hz and 1292 Hz.
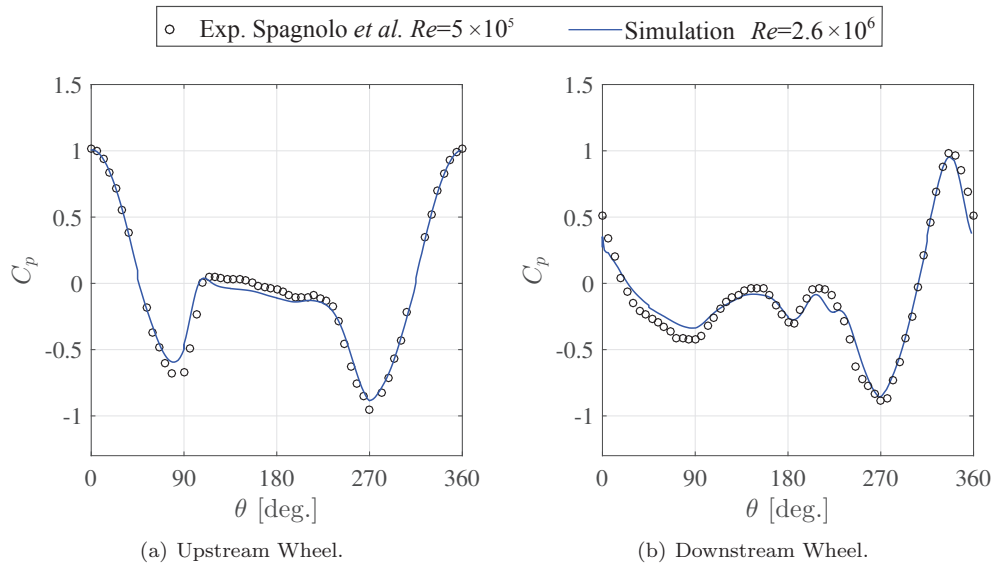
American Institute of Aeronautics and Astronautics

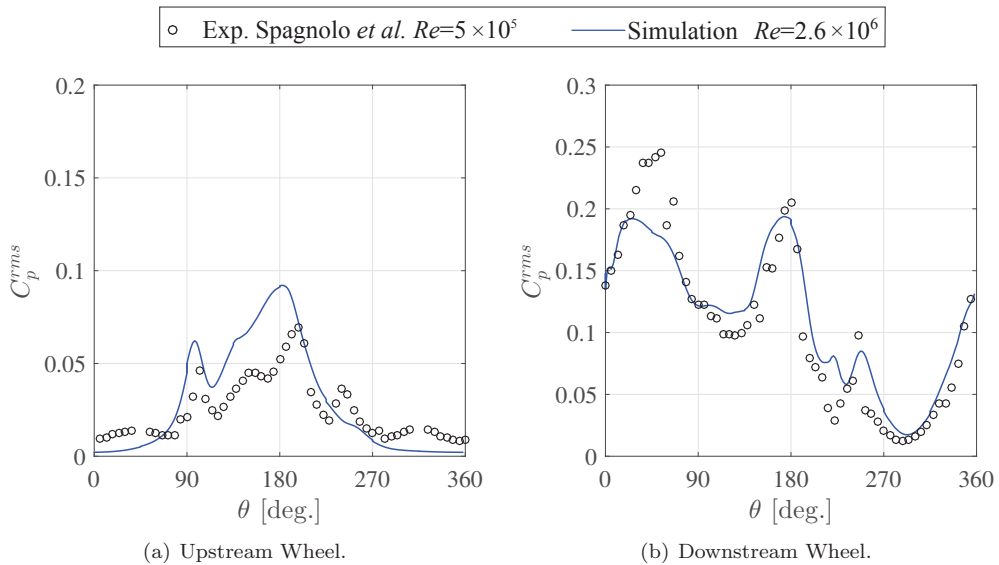Figure 6. Mean pressure coefficient C_p on the centreline ($z/D = 0$) of the upstream and downstream wheels.

Figure 7. Pressure coefficient RMS C_p^{rms} on the centreline ($z/D = 0$) of the upstream and downstream wheels.

American Institute of Aeronautics and Astronautics

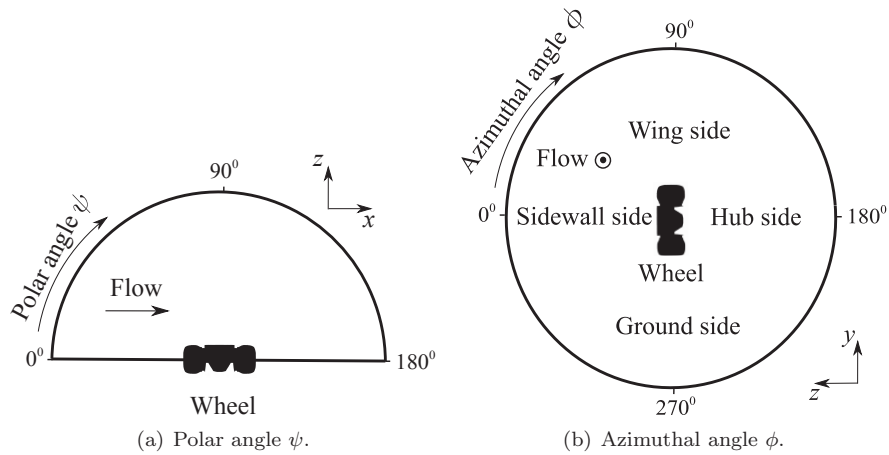(a) Polar angle ψ.

(b) Azimuthal angle ϕ.

Figure 8. Schematic of observer angles with respect to the upstream wheel centre. The hub side observer, sidewall side observer and ground side observer refer to the positions of $(\psi = 90°, \phi = 180°)$, $(\psi = 90°, \phi = 0°)$ **and** $(\psi = 90°, \phi = 270°)$, **respectively.**

The far-field acoustics from the upstream wheel and downstream wheel at three observer positions (hub side, sidewall side and ground side) are compared to the isolated single wheel case given by Wang *et al.*[8] in Figure 9. The frequency scale is divided into a low frequency range ($f < 400$ Hz), a middle frequency range (400 Hz $< f <$ 2000 Hz) and a high frequency range ($f > 2000$ Hz). Firstly, by comparing the upstream wheel noise with the single wheel noise at the hub side (Figure 9(a)), the middle frequency and high frequency spectral levels are shown to be comparable. The middle frequency and high frequency upstream wheel noise is mainly generated by the hub and rim cavities,[8] where the flow field is less effected by the presence of the downstream wheel. The difference between the upstream wheel noise and the single wheel noise is mostly in the low frequency range. This low frequency difference is caused by the large-scale flow interactions. This difference is larger at the hub side (Figure 9(a)) and sidewall side (Figure 9(b)) and is relatively smaller at the ground side (Figure 9(c)), which indicates that the interaction noise has a favourable side radiation direction as discussed previously and attributed to the shear layer flapping mode in the side direction. A small spectral hump is shown at $St_W = 0.21$ in the isolated single wheel case at the hub side (Figure 9(a)) and sidewall side (Figure 9(b)), causing a side force dipole pattern. This hump becomes more prominent and moves to $St_W = 0.19$ in the tandem wheels case. The decrease in frequency is likely due to a wider wake of the upstream wheel due to the presence of the downstream wheel, resulting in a lower shedding frequency. A similar phenomenon is seen for tandem cylinders, where the vortex shedding frequency of tandem circular cylinders can be less than for an isolated circular cylinder.[27]

(a) Hub side.

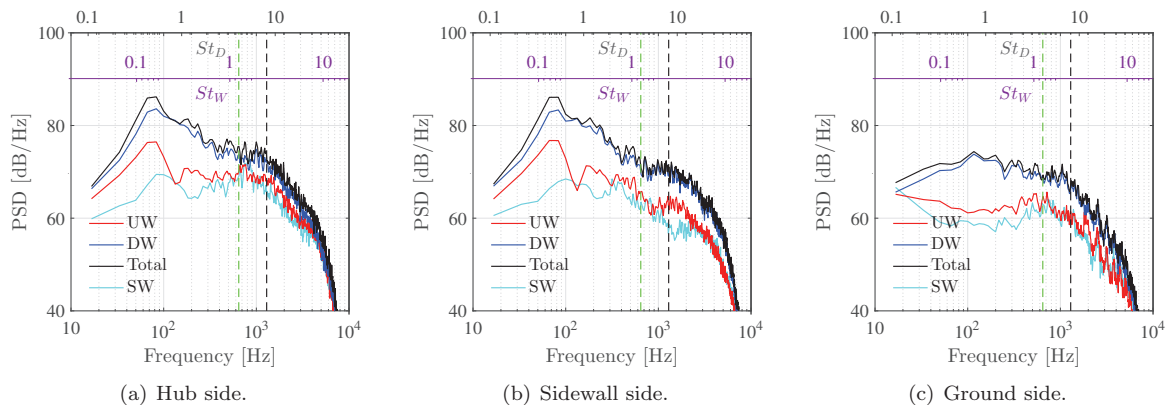(b) Sidewall side.

(c) Ground side.

Figure 9. Far-field acoustics from the Upstream Wheel (UW), Downstream Wheel (DW) and both wheels (Total), in comparison with the isolated Single Wheel (SW) case. --- **first depth mode (646 Hz),** --- **second depth mode (1292 Hz).**
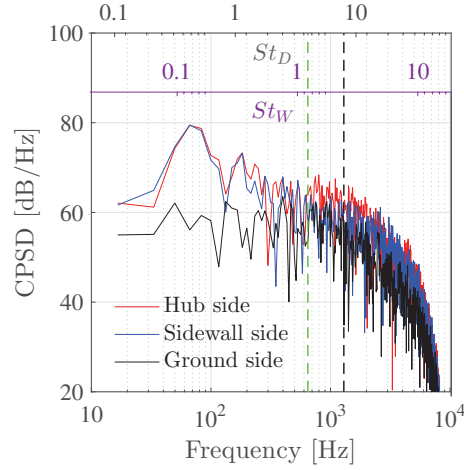
Figure 10. CPSD of the far-field acoustics at three different observer positions, using the upstream wheel and down-stream wheel acoustic data. - - - first depth mode (646 Hz), - - - second depth mode (1292 Hz).

Secondly, at all the three observer locations, the downstream wheel noise dominates the upstream wheel noise, especially in the low and middle frequency ranges. The downstream wheel noise in the middle frequency range (centred around the hub cavity depth modes) at the hub side and the sidewall side shares similar spectral profiles and levels, whereas the hub side middle frequency noise is louder than the sidewall side middle frequency noise in the isolated single wheel case, where the middle frequency noise is dominated by the first and second cylindrical cavity depth modes.[7,8] This suggests that, in the tandem wheels configuration, the middle frequency downstream wheel noise is generated by both flow interactions and hub cavity resonances (depth modes). By comparing the downstream wheel noise with the single wheel noise, the interaction noise shows a broadband spectrum, radiating more to the two side directions. The cross power spectral density (CPSD) (only absolute values) of the upstream wheel acoustics and the downstream wheel acoustics at three observer locations is shown in Figure 10. The CPSD is a measure of the coherence and phase shift of two signals, which is used to indicate flow and acoustic interactions, as the interactions give non-zero cross power at the interaction frequency. In Figure 10, the spectral peak at $St_W = 0.19$ only occurs in the two side directions. This spectral peak is generated by the flapping shear layer mode in the gap, as was shown in Section IV.C. At the ground side in Figure 10, the CPSD level in the low frequency range is lower than the levels in the other two side directions, since the interaction noise radiates less to the ground side.

The contour of OASPL against the polar angle ψ and azimuthal angle ϕ is provided in Figure 11, and a side force dipole is clearly depicted. This side force dipole directivity has also been shown by the spectral plot of the side force coefficient in Figure 3, which is due to the shear layer flapping in the gap and alternative impingements on the two side faces of the downstream wheel.
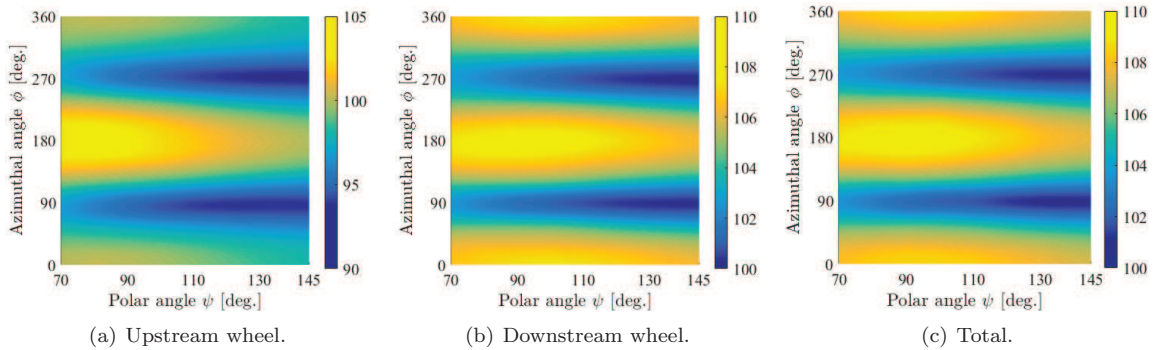

(a) Upstream wheel. (b) Downstream wheel. (c) Total.

Figure 11. Directivity of OASPL [dB] against polar angle ψ and azimuthal angle ϕ.

The directivity of narrowband SPL (with a band width of 8 Hz) at different frequencies is plotted in Figure 12 to give an insight into how the radiation patterns vary with frequency. Firstly at 20 Hz ($St_D = 0.13$) in
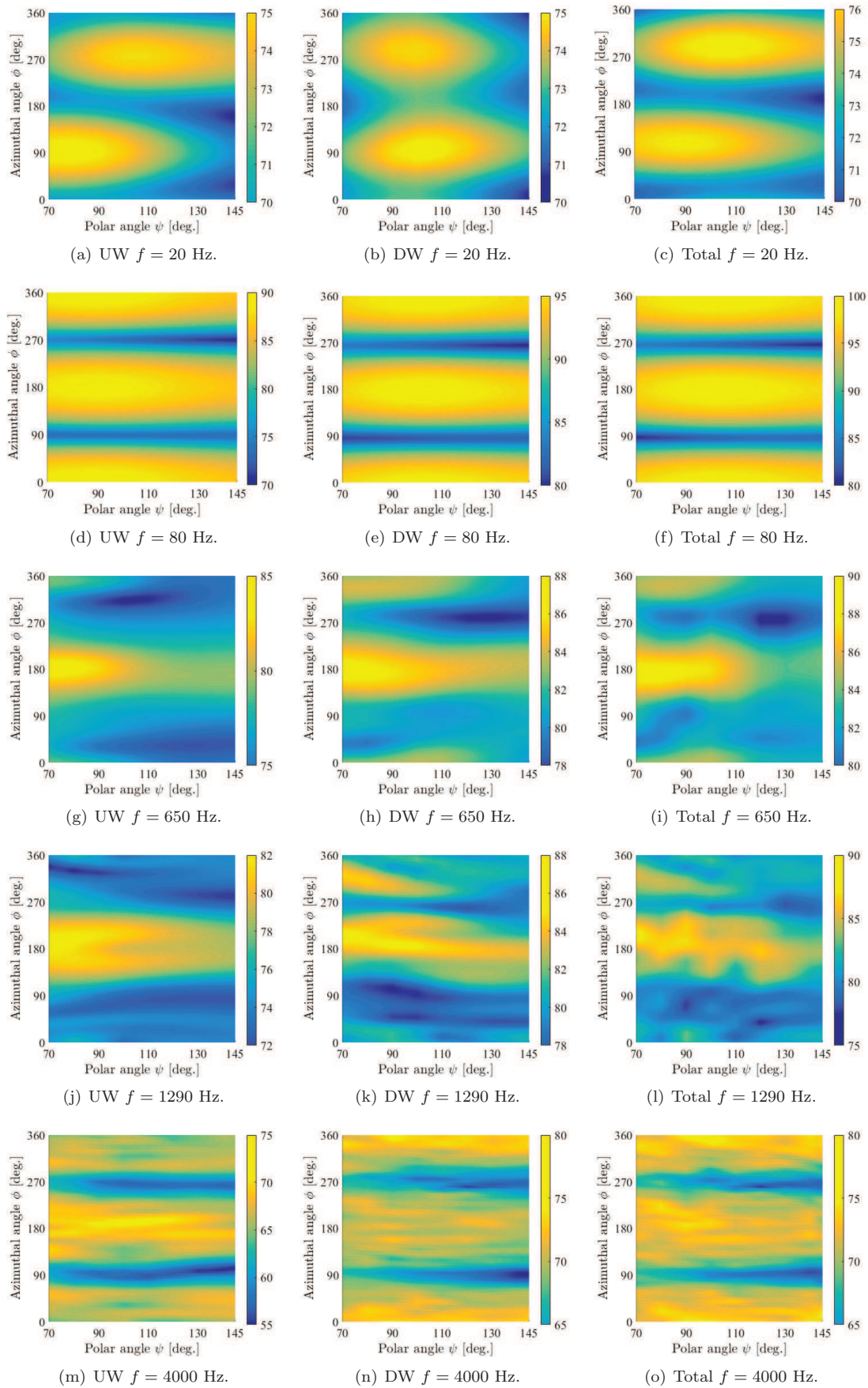
American Institute of Aeronautics and Astronautics

(a) UW $f = 20$ Hz.

(b) DW $f = 20$ Hz.

(c) Total $f = 20$ Hz.

(d) UW $f = 80$ Hz.

(e) DW $f = 80$ Hz.

(f) Total $f = 80$ Hz.

(g) UW $f = 650$ Hz.

(h) DW $f = 650$ Hz.

(i) Total $f = 650$ Hz.

(j) UW $f = 1290$ Hz.

(k) DW $f = 1290$ Hz.

(l) Total $f = 1290$ Hz.

(m) UW $f = 4000$ Hz.

(n) DW $f = 4000$ Hz.

(o) Total $f = 4000$ Hz.

Figure 12. Directivity of narrow band SPL [dB] against polar and azimuthal angles at different typical frequencies.

American Institute of Aeronautics and Astronautics

Figures 12(a), 12(b) and 12(c), the peak directivity is towards the wing side ($\phi = 90°$) and the ground side ($\phi = 270°$), which shows a lift dipole pattern (aligned with y axis). However, this lift dipole is asymmetric with respect to the horizontal plane $\phi = 180°$, due to the asymmetric mean flow field around the tandem wheels as discussed in the aerodynamic results. At the flow interaction frequency of $f = 80$ Hz ($St_W = 0.19$) in Figures 12(d), 12(e) and 12(f), the directivity still shows a dipole pattern but the favourable direction changes to the sidewall side ($\phi = 0°$) and hub side ($\phi = 180°$), representing a side force dipole pattern (aligned with the z axis), since the flow interactions are mainly on the side plane. The directivity at $St_W = 0.19$ also determines the OASPL directivity in Figure 11. At $f = 650$ Hz (first hub cavity depth mode) and $f = 1290$ Hz (second hub cavity depth mode), the hub cavity noise of the upstream wheel demonstrates similar directivity patterns to the isolated single wheel case by Wang *et al.*[8] This directivity shows a favourable sound radiation direction to the hub side, since the hub cavity depth modes are the major noise sources in this middle frequency range. However, the downstream wheel noise at these two hub cavity depth modes is more effected by the flow interactions than the upstream wheel noise, and the directivity pattern is more distorted. At $f = 4000$ Hz, the directivity is again dipole in nature, radiating towards both the sidewall and hub sides, mostly due to the small-scale fluctuations due to the rim cavities.[8]

IV.F.   Effects of covering the downstream wheel hub and rim cavities

In the isolated single wheel study by Wang *et al.*,[8] it has been shown that the hub cavity and rim cavities are the dominant middle frequency and high frequency noise sources, respectively. In this paper, the effects of downstream wheel hub and rim cavities on the far-field acoustics are investigated by simulating two additional configurations shown in Figure 13. The unmodified CADWIE wheel is the baseline configuration. A cross section through the baseline configuration is shown in Figure 13(a). The second configuration, **N**o **H**ub **C**avity (NHC), is shown in Figure 13(b), with the hub cavity covered. The geometry in this configuration is symmetrical with respect to $z/D = 0$ plane. The simulation of the NHC configuration aims to determine the contribution of the hub cavity to the far-field acoustics. The third configuration, NHCRC (**N**o **H**ub **C**avity and **R**im **C**avities), is shown in Figure 13(c). In this configuration, the hub cavity and the two rim cavities are covered. This configuration is essentially a short aspect ratio circular cylinder and can be compared with the NHC configuration to investigate the noise generated from the rim cavities. It should also be emphasised that, in these three cases, the upstream wheel has the baseline configuration and remains unmodified.
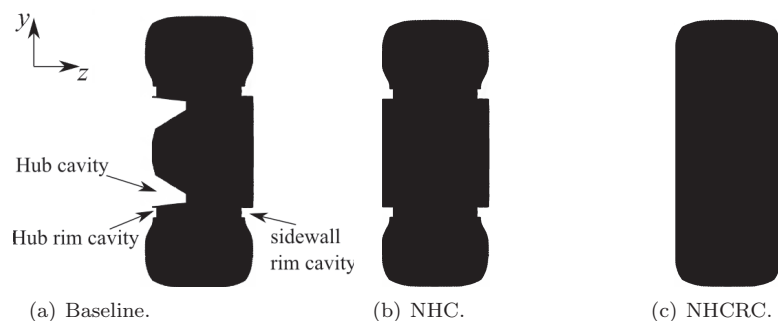

Figure 13. The cross section of three geometry configurations on the $x/D = 0$ plane, where the origin of the axes is at the wheel centre. (a) Baseline geometry; (b) No Hub Cavity (NHC) geometry; (c) No Hub Cavity and Rim Cavities (NHCRC) geometry.

The effect of covering the downstream wheel hub cavity and rim cavities on the downstream wheel noise is shown in Figure 14 at three different observer positions. At low frequencies, the three different configurations have comparable levels at all three observer locations, since the low frequency noise is mainly from flow interactions. There is a slight reduction in the middle frequency noise at the hub side (Figure 14(a)) in the NHC and NHCRC configurations. However, this reduction is not as much as that in the isolated single wheel case shown by Wang *et al.*,[8] since the wheel interactions are also significant contributors to this middle frequency noise. After covering the rim cavities (NHCRC), the spectrum at the ground side in Figure 14(c) demonstrates a reduction in the high frequency range, whereas the reduction is less distinguishable at the hub side and sidewall side. Compared to the hub cavity depth modes, the sideline acoustics are more dominated by the broadband flow interactions. Overall, the effect of downstream wheel hub cavity and rim cavities is not as significant as that in the isolated single wheel case (shown by Wang *et al.*[8]), and the flow

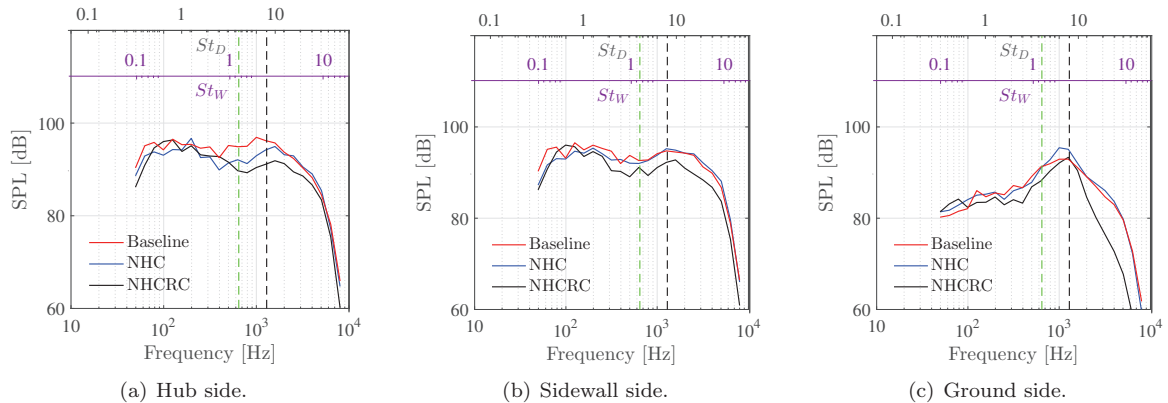American Institute of Aeronautics and Astronautics

Figure 14. Effects of covering the hub cavity (No Hub Cavity (NHC)) and both the hub and rim cavities (No Hub Cavity and Rim Cavities (NHCRC)) on the sound generated by the downstream wheel. The Sound Pressure Level (SPL) is plotted in one-third octave band frequencies. – – – first depth mode (646 Hz), – – – second depth mode (1292 Hz).

interactions are the dominant sources for the downstream wheel noise.

V. Conclusions

Previous simulations have shown that the hub cavity and rim cavities are the dominant noise sources of an isolated landing gear wheel in the middle and high frequency ranges, respectively.[7,8] In this work, high-order numerical simulations have been performed to study the flow interactions and noise sources of two landing gear wheels in tandem, with a separation distance of $L = 1.5D$. The wheel model is a high-fidelity configuration containing a hub cavity and two rim cavities, and this configuration is the same as the one used in the experiments by Zhang *et al.*[6] and numerical simulations by Wang *et al.*[7,8] The mean surface pressure coefficients were compared with the experimental measurements by Spagnolo *et al.*,[16] and good agreements were achieved. The RMS surface pressure coefficients showed reasonable agreements to the experimental data, and the discrepancies were hypothesised to be due to the different Reynolds numbers in the experimental and numerical cases and the boundary layer tripping used in the experiments. In the tandem configuration, the fluctuating side force dominates the fluctuating lift and drag forces, and a spectral peak at $St_W = 0.19$ was shown by the PSD of side force coefficient. The side force spectral peak is due to a flapping shear layer mode in the gap in the z direction and alternative flow impingements on the two side faces of the downstream wheel. The stagnation point on the downstream wheel surface is at $\theta = 335°$, and the mean flow field is asymmetric and a non-zero lift coefficient was shown in the simulation.

The downstream wheel is the dominant noise source, since it is immersed in the wake of the upstream wheel. The upstream wheel noise is comparable to the isolated single wheel noise in the middle and high frequency ranges, and the hub cavity depth modes are the major middle frequency noise sources for the upstream wheel. The flow interactions result in more low frequency noise with a spectral peak at $St_W = 0.19$. This interaction noise is radiated more towards the two sideline directions, where the upstream acoustics and downstream acoustics are more coherent compared to the ground side observer position. In this tandem configuration, the downstream wheel acoustic directivity at the hub cavity depth modes is more distorted than the upstream wheel due to the flow interactions. The effect of the downstream wheel hub and rim cavities on the far-field acoustics was isolated by covering them in the simulations, which showed that the flow interactions dominate the hub cavity resonances in the middle frequency downstream wheel noise generation. However, in the ground radiation direction, there was a reduction in the high frequency noise with both the hub and rim cavities covered, which was not achieved with just the hub cavity covered.

Acknowledgement

American Institute of Aeronautics and Astronautics

References

[1]Guo, Y., Yamamoto, K. J., and Stoker, R. W., "An Empirical Model for Landing Gear Noise Prediction," *10th AIAA/CEAS Aeroacoustics Conference*, AIAA 2004-2888, 2004.

[2]Liu, W., Kim, J. W., Zhang, X., Angland, D., and Caruelle, B., "Landing-Gear Noise Prediction Using High-Order Finite Difference Schemes," *Journal of Sound and Vibration*, Vol. 332, No. 14, 2013, pp. 3517–3534.

[3]Lockard, D. P., Khorrami, M., and Li, F., "Aeroacoustic Analysis of a Simplified Landing Gear," *10th AIAA/CEAS Aeroacoustics Conference*, AIAA 2004-2887, 2004.

[4]Casalino, D., Ribeiro, A. F., and Fares, E., "Facing Rim Cavities Fluctuation Modes," *Journal of Sound and Vibration*, Vol. 333, No. 13, 2014, pp. 2812–2830.

[5]Ribeiro, A., Casalino, D., and Fares, E., "CFD/CAA methods for landing gear noise prediction," *19th AIAA/CEAS Aeroacoustics Conference*, AIAA 2013-2256, 2013.

[6]Zhang, X., Ma, Z. K., Smith, M., and Sanderson, M., "Aerodynamic and Acoustic Measurements of a Single Landing Gear Wheel," *19th AIAA/CEAS Aeroacoustics Conference*, AIAA 2013-2160, 2013.

[7]Wang, M., Angland, D., Zhang, X., and Fattah, R., "High-Order Numerical Simulations of An Isolated Landing Gear Wheel with A Hub Cavity," *22nd AIAA/CEAS Aeroacoustics Conference*, AIAA 2016-2902, 2016.

[8]Wang, M., Angland, D., and Zhang, X., "The Noise Generated by a Landing Gear with Hub and Rim Cavities," *Journal of Sound and Vibration*, Vol. 392, 2017, pp. 127–141.

[9]Lockard, D. P., "Summary of the Tandem Cylinder Solutions from the Benchmark problems for Airframe Noise Computations-I Workshop," *49th AIAA Aerospace Sciences Meeting including the New Horizons Forum and Aerospace Exposition*, AIAA 2011-353, 2011.

[10]Spagnolo, S., Zhang, X., Hu, Z., Stalnov, O., and Angland, D., "Unsteady Aerodynamics of Single and Tandem Wheels," *Journal of Fluids and Structures*, Vol. 69, 2017, pp. 121–136.

[11]Oka, S., Kostic, Z. G., and Sikmanovic, S., "Investigation of the Heat Transfer Process in Tube Banks in Cross Flow," *International Seminar on Recent Development in Heat Exchangers*, 1972.

[12]Tanida, Y., Okajima, A., and Watanabes, Y., "Stability of a Circular Cylinder Oscillating in Uniform Flow or in a Wake," *Journal of Fluid Mechanics*, Vol. 61, No. 4, 1973, pp. 769–784.

[13]Igarashi, T., "Characteristics of the Flow around Two Circular Cylinders Arranged in Tandem : 1st Report," *Bulletin of JSME*, Vol. 24, No. 188, 1981, pp. 323–331.

[14]Ljungkrona, L., Norberg, C., and Sundén, B., "Free-Stream Turbulence and Tube Spacing Effects on Surface Pressure Fluctuations for Two Tubes in an In-Line Arrangement," *Journal of Fluids and Structures*, Vol. 5, No. 6, 1991, pp. 701–727.

[15]Spagnolo, S., Zhang, X., Hu, Z., and Angland, D., "Numerical Simulations of Single and Tandem Wheels for Aerodynamic Loads Prediction," *22nd AIAA/CEAS Aeroacoustics Conference*, AIAA 2015-3066, 2015.

[16]Spagnolo, S., *Unsteady Aerodynamic Loads on Aircraft Landing Gears*, Ph.D. thesis, University of Southampton, 2016.

[17]Spalart, P. R., Deck, S., Shur, M. L., Squires, K. D., Strelets, M. K., and Travin, A., "A New Version of Detached-eddy Simulation, Resistant to Ambiguous Grid Densities," *Theoretical and Computational Fluid Dynamics*, Vol. 20, No. 3, 2006, pp. 181–195.

[18]Kim, J. W., "Optimised boundary compact finite difference schemes for computational aeroacoustics," *Journal of Computational Physics*, Vol. 225, No. 1, 2007, pp. 995–1019.

[19]Kim, J. W., "High-order compact filters with variable cut-off wavenumber and stable boundary treatment," *Journal of Computers and Fluids*, Vol. 39, No. 7, 2010, pp. 1168–1182.

[20]Wang, M., Fattah, R., Angland, D., and Zhang, X., "High-Order Hybrid Cell-Centered Method for Computational Aeroacoustics," *21st AIAA/CEAS Aeroacoustics Conference*, AIAA 2015-3279, 2015.

[21]Sandberg, R. D. and Sandham, N. D., "Nonreflecting Zonal Characteristic Boundary Condition for Direct Numerical Simulation of Aerodynamic Sound," *AIAA Journal*, Vol. 44, No. 2, 2006, pp. 402–405.

[22]Li, J., Li, F., and E, Q., "A fully implicit method for steady and unsteady viscous flow simulations." *International Journal of Numerical Methods in Fluids*, Vol. 43, No. 2, 2003, pp. 147–163.

[23]Farassat, F., "Derivation of Formulations 1 and 1A of Farassat," Technical Report 214853, NASA Langley research center, 2007.

[24]Lockard, D. P., Khorrami, M. R., and Li, F., "High Resolution Calculation of a Simplified Landing Gear," *10th AIAA/CEAS Aeroacoustics Conference*, AIAA 2004-2287, 2004.

[25]Zdravkovich, M. M., Brand, V. P., Mathew, G., and Weston, A., "Flow Past Short Circular Cylinders with Two Free Ends," *Journal of Fluid Mechanics*, Vol. 203, 1989, pp. 557–575.

[26]Nomura, Y., Yamamura, I., and Inawashiro, S., "On the Acoustic Radiation from a Flanged Circular Pipe," *Journal of the Physical Society of Japan*, Vol. 15, No. 3, 1960, pp. 510–517.

[27]Summer, D., "Two Circular Cylinders in Cross-Flow: A Review," *Journal of Fluids and Structures*, Vol. 26, 2010, pp. 849–899.

American Institute of Aeronautics and Astronautics